文章编号: 1001 - 9014(2016)02 - 0184 - 06

DOI:10.11972/j.issn.1001 - 9014.2016.02.011

High selectivity millimeter wave band pass filter using novel dual-mode circular cavities

DUONG Tuan-Viet[1*], HONG Wei[1], HAO Zhang-Cheng[1], ZHUANG Jian-Xing[1], LE Trong-Hieu[1], JIANG Mei[2]

(1. State Key Laboratory of Millimeter Waves, School of Information Science and Engineering, Southeast University, Nanjing 210096, China;
2. Science and Technology on Electromagnetic Scattering Laboratory, Shanghai 200438 China)

Abstract: A novel method for the realization of high selectivity millimeter wave band pass filters is presented. A small perturbing notch was etched at sidewall of a dual-mode circular cavity to improve cross coupling between two orthogonal modes. By properly changing the perturbing angle, the bandwidth is expanded and location of the transmission zero can be easily adjusted to significantly enhance the filter selectivity. The V-band filters have been designed, fabricated and measured. The experiment results showed an excellent agreement with simulation results. Unlike conventional filters, the proposed prototypes do not need any additional mechanical tuning element. It has merits of simple design process, high selectivity, compact size and quasi-planar structure.

Key words: circular cavity, dual-mode, filter, mm-wave, transmission zero
PACS: 84.40-x, 07.57. Pt

基于新型双模圆谐振腔的高选择性毫米波滤波器

杨俊越[1*], 洪 伟[1], 郝张成[1], 庄建兴[1], 黎重孝[1], 江 梅[2]

(1. 东南大学 信息科学与工程学 院毫米波国家重点实验室,江苏 南京 210096;
2. 电磁散射重点实验室,上海 200438)

摘要:提出了一种新颖的高选择性毫米波带通滤波器及其设计方法.在圆谐振腔的侧壁加入槽型微扰结构,通过调节微扰小槽的角度可以控制滤波器带外传输零点的位置,从而实现了带宽可调、高选择性的双模圆谐振腔带通滤波器.根据该滤波器结构、理论分析和仿真设计基础,研制了在V波段滤波器样品并进行了测试.实验结果与方正吻合得良好.与传统双模圆腔滤波器相比,所提出的滤波器不需要额外的调节结构,其设计方法简单,选择特性高,结构紧凑,具有一定的工程价值用于高性能平面化毫米波滤波器的设计.

关 键 词:圆腔;双模;滤波器;毫米波;传输零点

中图分类号:TN713.5 **文献标识码**:A

Introduction

Recently, dual-mode circular cavity (DMCC) attracts much attention for high performance band pass filter (BPF) applications due to their higher selectivity, smaller size and less mass than conventional single-mode direct coupled filters[1]. In the conventional DMCC filter, in order to reduce the time-consuming tuning process and production cost, some works have been reported to remove tuning-screw system. For example, a ridged circular waveguide section has been proposed as shown in Fig. 1 (a)[2]. In addition, the mm-wave dual-mode substrate integrated waveguide diplexer have been presented[3], wherein circular and elliptic cavities with adjustable angle between input and output ports are adopted to achieve

Received date: 2015 - 04 - 27, **revised date**: 2015 - 12 - 17 **收稿日期**:2015 - 04 - 27, **修回日期**:2015 - 12 - 17
Foundation items: Supported bySpecialized Research Fund for the Doctoral Program of Higher Education of China(20120092110012), and National Natural Science Foundation of China(61471118)
Biography: DUONG Tuan-Viet (1980-), male, Ha Noi, Vietnam, Ph. D. Research interests include areas of microwave and mm-wave applications, the solid-state devices and circuits.
* **Corresponding author**: E-mail: vietroc04@ gmail. com

the good selectivity as in Fig. 1(b). Although these filters and diplexer own the advantages of low cost, high integration capability, then the impact structure, insertion loss and selectivity still need to be improved further.

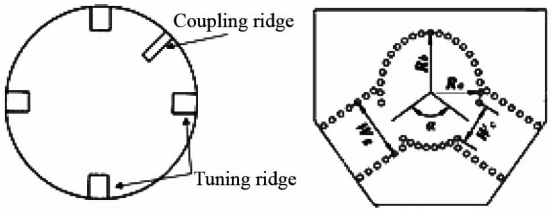

Fig. 1　Various tuning arrangements for DMCCfilters
图 1　各种双模滤波器的区别配置

In this paper, a novel method for design the high selectivity BPFs was proposed using a small perturbation notch etched on sidewall of the DMCC. As illustrated in Fig. 2, by properly adjusting the perturbing β angle, a controllable transmission zero (TZ) can be obtained to improve the selectivity and expand the filter bandwidth. The mm-wave selectivity-improved BPFs were analysed, designed and verified by experiment results.

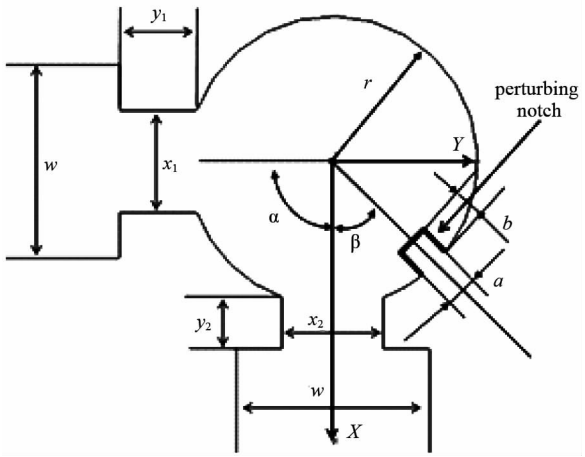

Fig. 2　Configuration of the proposed DMCC filter
图 2　建议 DMCC 滤波器的结构

1　Adjustable TZs and expanded bandwidth

The layout of the proposed filter using a perturbed DMCC is shown in Fig. 2, which consists of the rectangular waveguides as input/output ports, inductive windows, and a notched DMCC. The perturbed DMCC with the r radius supports two orthogonal resonating modes TM_{110}-like. The angle between the input and output ports is α, while β is the angle between the output port and the perturbing notch. The whole structure has the same height.

In the traditional cavity filter design[4], α is usually selected as 180°. However, for any $\alpha < 180°$, a weak coupling between input and output is produced, as discussed in Ref. [3]. In our initial design, the angle α is selected as 90°. As a result, the first TZ generated at *fz_1a* as in Fig. 3 can enhance the upper out-of-band attenuation of the proposed filter.

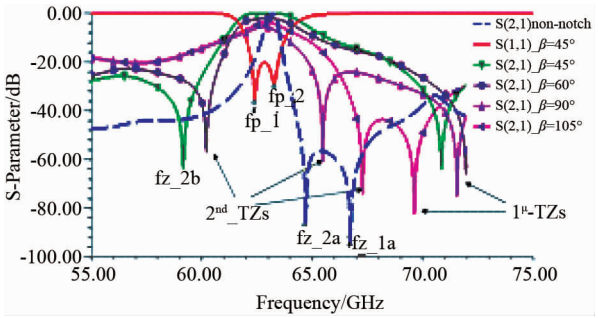

Fig. 3　Simulated response of the proposed filter versus angle β
图 3　建议滤波器的响应仿真结果随着角度 β 的变化

When the DMCC is operated without coupling notch, the frequency space between two orthogonal modes is very close, introducing an extremely narrow bandwidth. Although such a space can be slightly expanded using asymmetric inductive coupling windows, which giving a small cross coupling to generate the *fz_2a* TZ[4], the BPF still seriously suffers from the bandwidth limitation.

To overcome this disadvantage, a perturbing notch is etched at the sidewall of the DMCC at the initial β = 45°. In addition, the achieved additional cross coupling affects to the second TZ that shifted to *fz_2b* as in Fig. 3. This can be used to improve the selectivity of the proposed filter. The second TZ can be adjusted by tuning the perturbing angle. This is investigated with the help of the full-wave electromagnetic simulator HFSS. Figure 4 shows the influence of the second TZ location when the perturbing angle varies from 45° to 105°. As the β angle increases, the TZ shifts to higher frequency. Hence, by properly choosing the perturbing angle, the second TZ can be deliberately located at left passband slope when β = 45° or 60°, where as at right slope when β = 90° or 105°. It should be noted that the first TZ generated by α angle, always located at the upper stopband.

The electrical field distributions at resonant peaks, i. e. *fp_1b* and *fp_2b* in Fig. 3, are shown in Fig. 4, where two orthogonal resonating modes can be observed and the cross coupling between modes can be tuned by adjusting the perturbation notch.

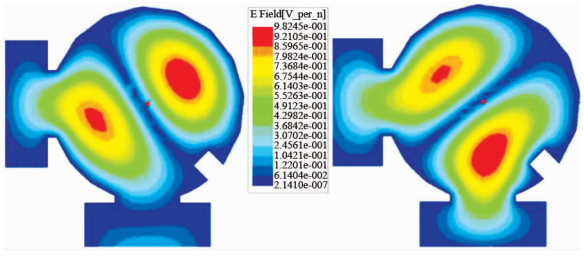

Fig. 4　Electric field distribution of two resonant modes at β = 45°
图 4　谐振双模的电场分布立在 β = 45°

2　Filter implementation

The perturbed-DMCC has been used to design V-

band BPFs in this section. Figure 2 depicts the layout of the 2nd-order single-DMCC filter (named BPF1), while Fig. 5 depicts the layout of the 4th-order dual-cavity filter (named BPF2). In order to support the V-band operation frequency only with the TE_{10} dominant mode, the input/output waveguides are selected as WR-15 standard, which giving $w \times h$ as 3.76 mm × 1.88 mm. The height of the whole structure is chosen as 1.88 mm to easily connect among cavities and the input/output ports. The size of the proposed cavity is determined by the operation frequency of the BPF, which can be evaluated by using the following equation:

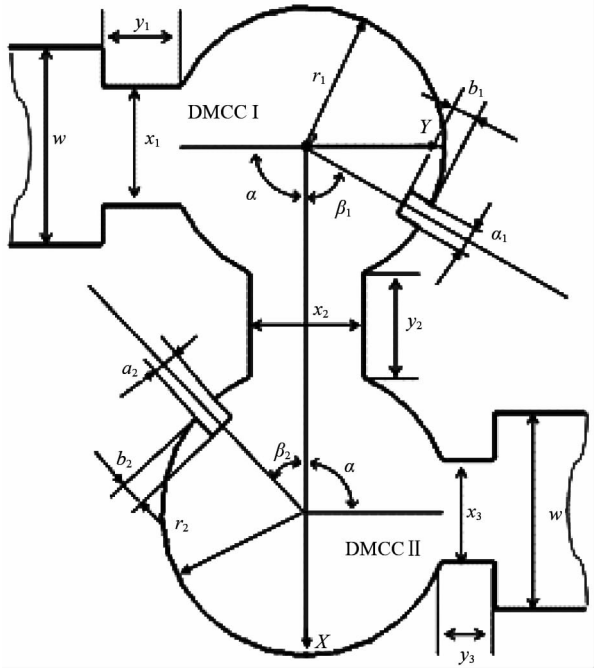

Fig. 5 Geometry parameters of implemented dual-cavity filter
图5 实现双腔滤波器的几何参数

$$f_{(\mathrm{TM}_{110})} = \frac{c}{2\pi} \cdot \frac{p_{\mathrm{nm}}}{r} \quad , \quad (1)$$

where c is the light velocity in free space, r is the radius of the DMCC. The $p_{\mathrm{nm}} = 3.832$ for the TM_{110} modes. To support the operation frequency around 65 GHz, the initial radius of the DMCCI is evaluated as 2.66 mm. This value will be adjusted to achieve the expanded bandwidth. Inductive coupling windows and the rectangular waveguide connecting DMCCs in the BPF2 are placed in orthogonal direction, i.e. fixed angle $\alpha = 90°$. While in the BPF1, angle $\alpha = 80°$, these ensure that first TZs are located at upper stopbands. The connecting waveguide width is chosen to be smaller than the DMCCs radii. In initial our design, the connecting waveguide size is 2 mm × 3.5 mm, while the input/output windows sizes are 2 mm × 1 mm.

The Eigenmode Solver of HFSS simulator has been used to investigate resonating modes of the perturbed-DMCC BPFs. For the high-order filter design, the adopted cavities usually need to be resonated with different resonating frequencies to support wideband applications. Typically, in the BPF2, the DMCC I supports the second and fourth resonant modes, while the DMCC II supports the first and third modes. Figure 6 shows the frequency deviation of four modes from the 65 GHz center frequency when $r_1 = 2.66$ mm and r_2 is varied from $1.038 \cdot r_1$ to $1.052 \cdot r_1$. It can be seen that, the larger the radius r_2, then the larger the deviation of the fourth mode (Delta4 line), while that of the first mode (Delta1 line) is mostly unchanged and the wider bandwidth. Therefore, to satisfy the specifications of the high-order filter, the radii of the proposed cavities are chosen as $r_1 = 2.66$ mm and $r_2 = 2.78$ mm.

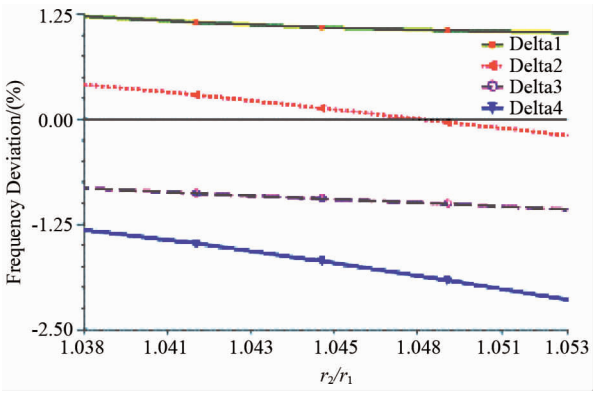

Fig. 6 Frequency deviation of resonant modes versus radius
图6 谐振模式的频率偏差随着半径的变化

The general coupling schematic of proposed perturbed-DMCC filters is shown in Fig. 7, where each node represents a resonant mode; S and L denote the source and load nodes, respectively. This topology contains not only the cross coupling between nodes, the source and load coupling to nodes, but also a direct coupling between the source and the load[6]. Figure 8 shows the extended general coupling reciprocal matrix of BPF2, where a direct coupling between the source and the load can be computed in term of scattering parameter S_{21}

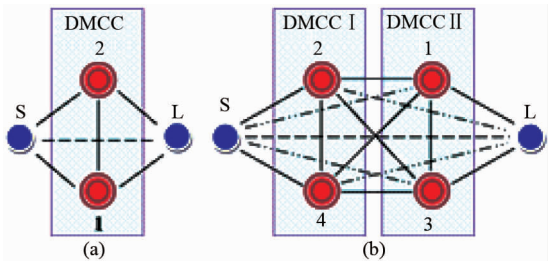

Fig. 7 General coupling topology of (a) BPF1, and (b) BPF2
图7 (a)BPF1,(b)BPF2 的综合耦合拓扑

$$\boldsymbol{M} = \begin{bmatrix} 0 & \boldsymbol{M}_{S1} & \boldsymbol{M}_{S2} & \boldsymbol{M}_{S3} & \boldsymbol{M}_{S4} & \boldsymbol{M}_{SL} \\ \boldsymbol{M}_{1S} & 0 & \boldsymbol{M}_{12} & \boldsymbol{M}_{13} & \boldsymbol{M}_{14} & \boldsymbol{M}_{1L} \\ \boldsymbol{M}_{2S} & \boldsymbol{M}_{21} & 0 & \boldsymbol{M}_{23} & \boldsymbol{M}_{24} & \boldsymbol{M}_{2L} \\ \boldsymbol{M}_{3S} & \boldsymbol{M}_{31} & \boldsymbol{M}_{32} & 0 & \boldsymbol{M}_{34} & \boldsymbol{M}_{3L} \\ \boldsymbol{M}_{4S} & \boldsymbol{M}_{41} & \boldsymbol{M}_{42} & \boldsymbol{M}_{43} & 0 & \boldsymbol{M}_{4L} \\ \boldsymbol{M}_{LS} & \boldsymbol{M}_{L1} & \boldsymbol{M}_{L2} & \boldsymbol{M}_{L3} & \boldsymbol{M}_{L4} & 0 \end{bmatrix}$$

Fig. 8 General coupling matrix of the BPF2
图8 BPF2 的综合耦合矩阵

$$M_{SL}=\frac{1-\sqrt{1-|S_{21}|^2}}{|S_{21}|} \quad . \quad (2)$$

The M_{Si} and $M_{Lj}(i=1..4;j=1..4)$, denoting couplings between the source and load to each mode, can be extracted from external quality factors by

$$Q_{e,Si}=\frac{1}{M_{Si}^2\cdot \mathrm{FBW}};Q_{e,Li}=\frac{1}{M_{Li}^2\cdot \mathrm{FBW}} \quad . \quad (3)$$

Meanwhile, the cross coupling between resonant modes can be calculated from the following equation[6]

$$M_{ij}=M_{ji}=k(i,j)=\frac{1}{2}\left(\frac{f_{0j}}{f_{0i}}+\frac{f_{0i}}{f_{0j}}\right)\times\sqrt{\left(\frac{f_{pj}^2-f_{pi}^2}{f_{pj}^2+f_{pi}^2}\right)^2-\left(\frac{f_{oj}^2-f_{oi}^2}{f_{oj}^2+f_{oi}^2}\right)^2} \quad , \quad (4)$$

where, f_{0i} and f_{0j} are uncoupled self-resonant frequencies, f_{pi} and f_{pj}, are characteristics frequencies of coupled resonators. For the designed DMCC filter with different radii, Eq. 4 is applicable for both synchronously ($f_{0i}=f_{0j}$ in each DMCC) and asynchronously tuned ($f_{0i}/f_{0j}=1.006$ for TE_{11} dominant mode in different DMCCs). In our initial design of BPF2, the perturbing angles were chosen as $\beta_1=90°$ and $\beta_2=30°$. Using Eq. 4, firstly the coupling coefficients $k(i,j)$ of resonators were analyzed versus the connecting window width and then versus notches sizes. The results are illustrated in Figs. 9 and 10, respectively. As shown in Fig. 9, the larger width of center window leads to the more degraded $k(1,4)$ of two asynchronously tuned coupled resonators in two different cavities, while the others change unremarkably. At $x_2/r_1=0.75$, the coupling $k(1,4)$ is the strongest, both $k(1,3)$ of cavity II and $k(2,4)$ of cavity I are approximately 0.02, whereas $k(1,2)$, $k(2,3)$, $k(3,4)$ around 0.01 are the smallest. Fig. 10 shows that the stronger coupling $k(2,4)$ of two synchronously tuned coupled orthogonal resonators in cavity *I* can be obtained using the larger perturbation notch, while the coupling coefficient $k(1,3)$ in the cavity *II* keeps unchanged. As a consequence, in order to obtain desired coupling coefficients, $x_2/r_1=0.75$, $y_2/r_1=1.32$, $a_1/r_1=0.145$, $b_1/r_1=0.19$ were adopted in our design.

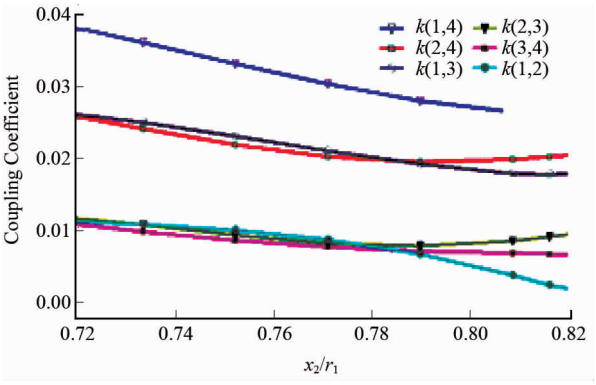

Fig. 9　Coupling coefficient of resonant modes versus x_2

图 9　谐振模式的耦合系数随着 x_2 的变化

As discussed above, the locations of TZs can be adjusted by tuning the perturbation angles of the notches,

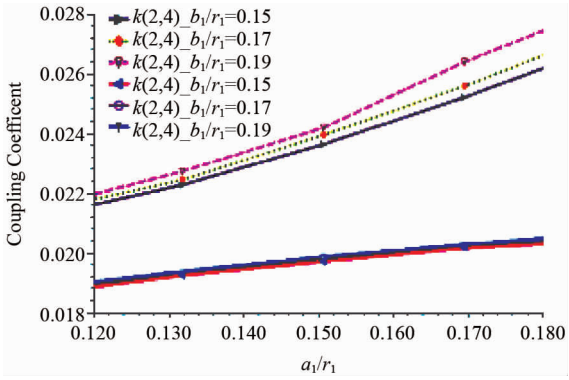

Fig. 10　Coupling coefficient of resonant modes versus a_1 and b_1

图 10　谐振模式的耦合系数随着 a_1 和 b_1 的变化

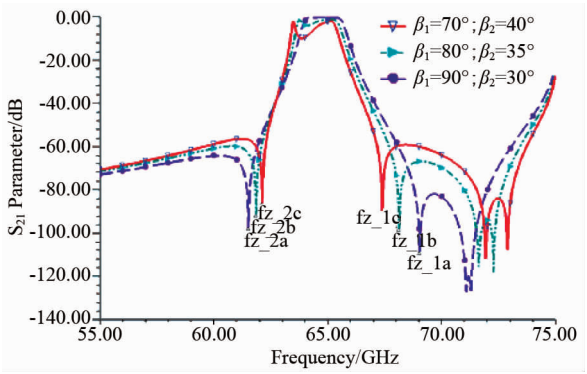

Fig. 11　Simulated S_{21} of the BPF2 versus perturbing angle

图 11　BPF2 的仿真 S_{21} 随着扰动角度的变化

i. e. β_1 and β_2. Figure 11 shows the simulated S_{21} parameter of the BPF2 with varied coupling angles. Each DMCC can provide two TZs that can be found in the S_{21} responses. The perturbation of cavity I was used to generate the first TZ at upper stopband. By reducing the perturbing angle β_1 of in cavity I, this TZ can be tuned to close the passband right slope. The perturbing notch in cavity II was used to generate the second TZ at lower stopband. By increasing the angle β_2, the TZ can be shifted to the passband left slope. Consequently, two TZs can be designed at both side of passband. Therefore, a high selectivity can be obtained.

Table 1　Physical dimension of the V-band BPF1

表 1　V-band BPF1 的物理尺寸

Symbol	Evaluated Value	Optimized Value	Unit
w	3.759	3.759	mm
h	1.880	1.880	mm
x_1	2.000	1.830	mm
x_2	2.000	1.640	mm
y_1	1.000	0.710	mm
y_2	1.000	0.420	mm
r	2.800	2.656	mm
a	0.500	0.260	mm
b	0.500	0.260	mm
α	80	80	degree
β	80	80	degree

Table 2 Physical dimension of the V-band BPF2
表 2 V-band BPF2 的物理尺寸

Symbol	Evaluated Value	Optimized Value	Unit
w	3.759	3.759	mm
h	1.880	1.880	mm
x_1	2.000	2.292	mm
x_2	2.000	2.185	mm
x_3	2.000	1.940	mm
y_1	1.000	1.545	mm
y_2	3.510	3.540	mm
y_3	1.000	0.300	mm
r_1	2.660	2.656	mm
r_2	2.780	2.770	mm
a_1	0.385	0.245	mm
a_2	0.750	0.925	mm
b_1	0.500	0.445	mm
b_2	0.500	0.396	mm
β_1	90	85	degree
β_2	30	32	degree

$$M=\begin{bmatrix} 0 & 0.298 & -0.612 & 0.611 \\ 0.298 & 0 & 0.003 & -0.591 \\ -0.612 & 0.003 & 0 & -0.447 \\ 0.611 & -0.591 & -0.447 & 0 \end{bmatrix}$$

(a)

$$M=\begin{bmatrix} 0 & -0.182 & -1.397 & -0.936 & -1.009 & 0.180 \\ -0.182 & 0 & 0.006 & 0.018 & 0.269 & 0.182 \\ -1.397 & 0.006 & 0 & 0.017 & 0.021 & 0.990 \\ -0.936 & 0.018 & 0.017 & 0 & 0.009 & 0.516 \\ -1.009 & 0.269 & 0.021 & 0.009 & 0 & 0.675 \\ 0.180 & 0.182 & 0.990 & 0.516 & 0.675 & 0 \end{bmatrix}$$

(b)

Fig. 12 Extracted coupling matrices of (a) BPF1, and (b) BPF2
图 12 (a) BPF1 和 (b) BPF2 的提取耦合矩阵

Once all coupling coefficients and their corresponded geometries were obtained, a full-waves optimization process using HFSS simulator was carried on to satisfy the desired specifications for the design filters, including the 65 GHz center frequency, 1.2 dB insertion loss and bandwidth expanded to 2.5%. The value of the physical parameters of both topologies with structures presented in Figs. 2 and 5, before and after the optimization are shown in Tables 1 and 2, respectively. The finally general coupling matrices for filters were extracted as shown in Fig. 12. The finally simulated results of these filters are shown in Figs. 14 and 16. Two TZs were closely designed at the edges of passband, which greatly improves the selectivity of the filter. The dual-cavity filter has a spurious around 75 GHz, which is resulted from the high order mode TM_{210}.

3 Filter fabrication and measurement

The designed V-band single-cavity and the dual-cavity BPF prototypes have been fabricated by using the miller machining technology. Figure 13 is the photograph of the manufactured BPF1 with optimized physical parameters as Table 1, and its measurement results are shown in Fig. 14. Due to the slight deviation of processed sizes,

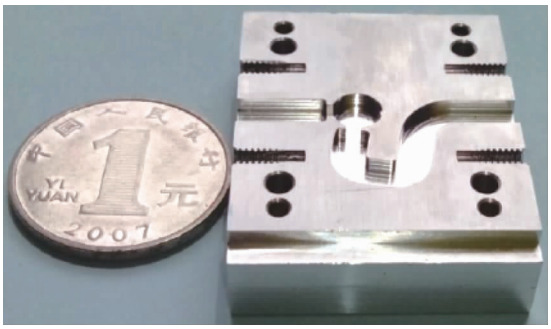

Fig. 13 Photograph of the fabricated BPF1
图 13 BPF1 制作实物的照片

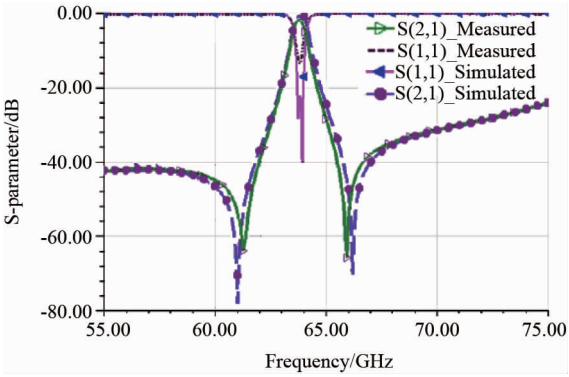

Fig. 14 Simulated and measured results of the BPF1
图 14 BPF1 的仿真与测试结果

a frequency shift is observed in passband of the filter[5]. Good agreement is obtained among simulated and measured results. The angle between input and output ports was designed as $\alpha = 80°$ to generate a TZ at 65.94 GHz closer to upper edge of passband. The perturbation angle is optimized as $\beta = 80°$ for generating another TZ at 61.31 GHz, which reach to low edge of the passband. Therefore, a high selectivity can be observed in Fig. 14. The measured results have an insertion loss of 1.8 dB at 63.84 GHz, and the narrow fractional bandwidth about 1%.

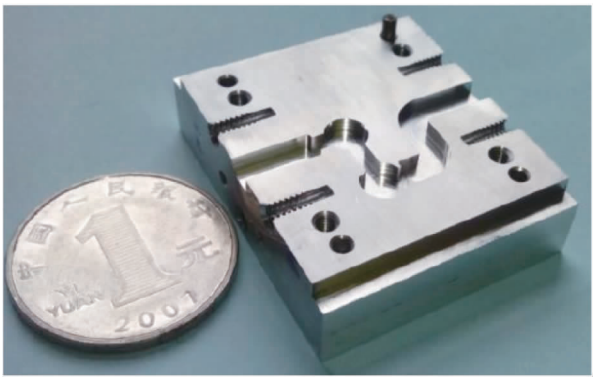

Fig. 15 Photograph of the fabricated BPF2
图 15 BPF2 制作实物的照片

The dual-cavity prototype was fabricated with the optimized geometries listed in Table 2. Fig. 15 shows photograph of the manufactured dual-cavity filter. The measured results compared with the simulated results are

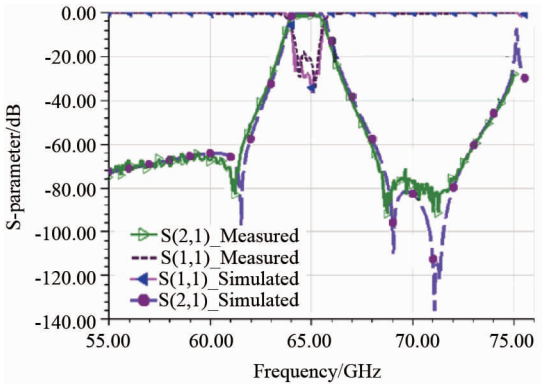

Fig. 16　Simulated and measured results of the BPF2
图 16　BPF2 的仿真与测试结果

shown in Fig. 16. Two TZs, which are individually resulted by the perturbing angles β_1, β_2 of notches, are located at 61.25 GHz and 68.6 GHz, respectively. The other TZs generated by the rotation angle $\alpha = 90°$ are located at upper stopband. The measured BPF2 has the expanded fractional bandwidth of 2.5%, 1.35 dB insertion loss of at center frequency of 64.8 GHz. The measured S_{11} is smaller than -20dB, and the out-of-band rejection is about 65dB.

4　Conclusion

This paper proposed a novel technique to design high selectivity BPFs with controllable transmission zeros, which does not need the sophisticated tuning screws for the filter tuning after fabrication. A small perturbation notch is provided for the filter application, which can be used to easily adjust the locations TZs to improve the selectivity of the filters. Two V-band filter prototypes have been designed, fabricated and measured. The experiment results confirm the good agreement with the simulated results, which shows that the proposed techniques are promising to design the compact and low cost mm-wave quasi-planar BPFs.

Acknowledgement

The authors appreciate the financial supported by Specialized Research Fund for the Doctoral Program of Higher Education of China, Grant No. 20120092110012, and the National Natural Science Foundation of China 61471118.

References

[1] Kudsia C, Cameron R, Tang W C. Innovations in microwavefilters and multiplexing networks for communications satellite systems [J]. *IEEE Trans. Microwave Theory Tech.*, 1992, **40**(6): 1133 - 1149.

[2] Guglielmi M, Molina R C, Melcon A A. Dual-mode circular waveguide filters without tuning screws [J]. *IEEE Microwave Guided Wave Lett.*, 1992, **2**(11): 457 - 458.

[3] Tang H J, Hong W, Chen J, *et al*. Development of millimeter-wave planar diplexers based on complementary characters of dual-mode SIW filters with circular and elliptic cavities [J]. *IEEE Trans. Microwave Theory Tech.*, 2007, **55**(4): 776 - 782.

[4] Guglielmi M, Jarry P, Kerherve E, *et al*. A new family of all-inductive dual-mode filters [J]. *IEEE Trans. Microwave Theory Tech.*, 2001, **49**(10): 1764 - 1769.

[5] ZHAO Xing-Hai, SHAN Guang-Cun, ZHENG Ying-Bin, *et al*. MEMS rectangular waveguide filter at 140 GHz [J]. *Journal of Infrared and Millimeter Waves* (赵兴海, 单光存, 郑英彬, 等. 140 GHz MEMS 矩形波导滤波器. **红外与毫米波学报**), 2013, **32**(2): 165 - 169.

[6] Hong J S. *Microstrip filter for RF/microwave applications* [M]. New Jersey: Wiley, 2011, 2nd, 193 - 231.

(上接 183 页)

ment in national forest inventories [J]. *Proc of the IUFRO Division*, 2009, **4**: 1 - 5.

[16] Ku N W, Popescu S C, Ansley R J, *et al*. Assessment of available rangeland woody plant biomass with a terrestrial LIDAR system [J]. *Photogrammetric Engineering & Remote Sensing*, 2012, **78**(4): 349 - 361.

[17] Lin Y, Jaakkola A, Hyyppä J, *et al*. From TLS to VLS: Biomass estimation at individual tree level [J]. *Remote Sensing*, 2010, **2**(8): 1864 - 1879.

[18] Liu X, Gavrilova M L, Rokne J. Incorporating object-centered sampling and Delaunay tetrahedrization for visual hull reconstruction [J]. *The Visual Computer*, 2009, **25**(5-7): 381 - 389.

[19] Luo X. Study on measuring of forest based on 3D laser scanning measurement [J]. *Beijing Forestry University*. 2006, **2**(8): 127 - 128.

[20] Maas H G, Bienert A, Scheller S, *et al*. Automatic forest inventory parameter determination from terrestrial laser scanner data [J]. *International journal of remote sensing*, 2008, **29**(5): 1579 - 1593.

[21] McDaniel M W, Nishihata T, Brooks C A, *et al*. Terrain classification and identification of tree stems using ground - based LiDAR [J]. *Journal of Field Robotics*, 2012, **29**(6): 891 - 910.

[22] Moorthy I, Miller J R, Berni J A J, *et al*. Field characterization of olive (Olea europaea L.) tree crown architecture using terrestrial laser scanning data [J]. *Agricultural and Forest Meteorology*, 2011, **151**(2): 204 - 214.

[23] Chun-li S, Peng H, Cheng-yi H, *et al*. The expatiation of delaunay algorithms and a promising direction in application [J]. *Science of Surveying and Mapping*, 2004, **29**(6): 68 - 71.

[24] Stoker J. Visualization of multiple-return Lidar data: Using voxels [J]. *Photogramm. Eng. Remote Sens*, 2009, **75**(2): 109 - 112.

[25] Vander Zande D, Stuckens J, Verstraeten W W, *et al*. Assessment of light environment variability in broadleaved forest canopies using terrestrial laser scanning [J]. *Remote Sensing*, 2010, **2**(6): 1564 - 1574.

[26] Waguchi Y. Accuracy and precision of crown profile, volume, and surface area measurements of 29-year-old Japanese cypress trees using a Spiegel relascope [J]. *Journal of forest research*, 2004, **9**(2): 173 - 176.

[27] Wei Y, Su X. Novel and fast mapping triangulation algorithm for unorganized points cloud [J]. *Optical Engineering*, 2008, **47**(11): 117205-117205 - 8.

[28] Xiong N N, Wang J, Luo X, *et al*. Measuring tree crown volume based on three dimension laser scanning and mapping system taking Pinus tabulaeformis as a case [J]. *Journal of Beijing Forestry University*, 2007, **29**(Suppl. 2): 61 - 65.